



Cite this: *J. Mater. Chem. B*, 2018, 6, 8137

Induction of mitochondrial apoptosis for cancer therapy *via* dual-targeted cascade-responsive multifunctional micelles†

Guoqing Wei, Yi Wang, Xuehui Huang, Guang Yang, Jingya Zhao and Shaobing Zhou *

Herein, we present a prodrug-loaded multifunctional polymer micelle with hyaluronidase/redox/light multilevel responses and with cell membrane/mitochondrion-dual targeting abilities. This nanocarrier can be internalized by tumor cells *via* CD44 receptor-mediated targeting. The encapsulated prodrug is released as the carrier is dissociated after the initial degradation of the hyaluronic acid layer by hyaluronidase, followed by the cleavage of the disulfide bonds between hydrophilic and hydrophobic segments in the micelle under the conditions of increased levels of GSH in the cytoplasm. The released prodrug can rapidly target the mitochondria *via* the TPP function, and convert to the free drug cisplatin through a redox-responsiveness effect. Simultaneously, the membrane permeability of the mitochondria can be improved by the generated reactive oxygen species (ROS) from light irradiation, thus allowing the entry of cisplatin into the mitochondria and causing mitochondrial damage, ultimately leading to mitochondria-mediated apoptosis. Consequently, this nanoformulation shows a highly effective anticancer efficacy *in vivo*.

Received 16th August 2018,
Accepted 9th November 2018

DOI: 10.1039/c8tb02159g

rsc.li/materials-b

Introduction

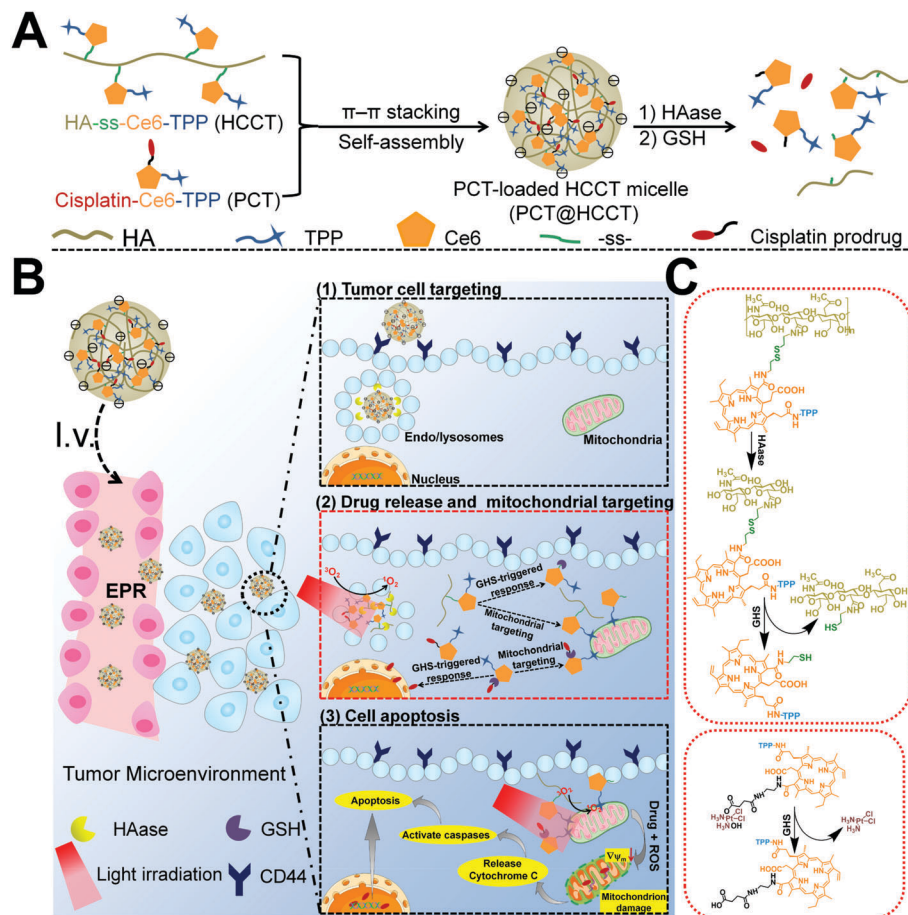
Subcellular-targeted therapy has become an important emerging area for cancer treatment with the development of biomedical nanotechnology.^{1–3} As compared to the random interaction of drugs in the cell, the therapeutic effect should be enhanced many-fold if the drugs can be specifically directed toward the target organelle (*i.e.*, nucleus,^{4–6} mitochondria,^{7,8} or endoplasmic reticulum).^{9–11} As is commonly known, most of the anticancer drugs, such as camptothecin (CPT), doxorubicin (DOX), and cisplatin, have been used in clinical studies for antitumor therapy as DNA-damaging agents.^{12–15} Unfortunately, drugs targeting the nuclear genome usually show a low-therapeutic effect, because the DNA self-repairing pathway is always present in the nucleus.¹⁶ In contrast, mitochondrial DNA lacks the ability to self-repair, and may be more vulnerable to damage than nuclear DNA.¹⁷ In other words, DNA-damaging anticancer agents targeting mitochondrial DNA could present more advantages than drugs targeting the nuclear genome, which could enhance the therapeutic effect of anticancer drugs.¹⁸ Meanwhile, damaging mitochondria could lead to the release

of cytochrome *C* into the cytoplasm, and this would further activate a cascade of caspase-9 and caspase-3 reactions and promote tumor cell apoptosis *via* initiating the mitochondria-mediated apoptotic pathways.^{1,19–21} Therefore, the strategy for mitochondria-targeted therapy based on nanomedicine is an optimal choice for improving antitumor efficiency.

To achieve precise transport of drugs to mitochondria, mitochondrial targeting ligand functionalized nanocarriers (or drugs) have received increased attention.^{22–24} Among these targeting ligands, lipophilic cations—typically triphenylphosphine (TPP)—could efficiently attach to mitochondria owing to the increased mitochondrial membrane potential.^{16,22,25} Nevertheless, because the mitochondria have a hydrophobic and dense double-membrane system, the latter acts as a formidable barrier and prevents many bioactive compounds from gaining entry. Thus, most mitochondria-targeting prodrugs, or drug-loaded mitochondria-targeting nanoparticles, cannot damage the mitochondria of tumor cells.^{5,17} Therefore, it is of great importance to provide the nanoparticles or prodrugs with the ability to improve the permeability of the mitochondrial membrane after targeting the mitochondria. Photosensitizers, for instance Chlorin e6 (Ce6) (commonly used as a photodynamic therapy (PDT) agent), can transfer energy from light irradiation to surrounding dissolved oxygen (O₂) and generate therapeutic reactive oxygen species (ROS). This results in a significant decrease of mitochondrial membrane potential ($\Delta\Psi_m$) and a synchronous improvement of the membrane permeability *via* oxidizing unsaturated

Key Laboratory of Advanced Technologies of Materials, Ministry of Education, and School of Materials Science and Engineering, Southwest Jiaotong University, Chengdu, Sichuan 610031, P. R. China. E-mail: shaobingzhou@swjtu.edu.cn, shaobingzhou@hotmail.com

† Electronic supplementary information (ESI) available: Materials, experimental details, additional data, Table S1 and Fig. S1–S10. See DOI: 10.1039/c8tb02159g



Scheme 1 (A) Schematic illustrations of the formation of a PCT-loaded HCCT micelle (PCT@HCCT) via self-assembly and the dissociation of the micelle through the HAase/GSH sequential response process. (B) Schematic illustration of specifically inducing mitochondrial apoptosis for enhancing cancer therapy via the micelle: (1) membrane-targeting by receptor-mediated internalization; (2) drug release and mitochondrial targeting: HAase-induced HA degradation in endosomes and light irradiation-mediated *endo*/lysosomal escape; mitochondria targeting via TPP function and the improvement of membrane permeability by generated ROS from light irradiation, resulting in entry of the released cisplatin into mitochondria; (3) cell apoptosis resulting from the mitochondrial damage due to ROS and cisplatin. (C) The corresponding changes in the chemical structure of polymer HCCT by the sequential HAase- and redox-responsiveness and prodrug PCT in response to GSH.

phospholipids.^{8,24} However, the bioactivity of ROS is restricted to an extremely small spherical region centered at the point of its primary generation, owing to their short lifetimes (~ 40 ns) and short diffusion range (≈ 20 nm).^{26,27} To utilize the biological activity of ROS in a more efficient manner and improve antitumor effects, there is an urgent need to develop a new drug delivery system, which can directly carry the therapeutic agent into the mitochondria to induce mitochondrial apoptosis.

Accordingly, in this study, we developed a newly multifunctional micelle (termed HCCT) with hyaluronidase, redox, and light multilevel responses, and cell membrane- and mitochondrion-dual-targeting functions. This micelle can encapsulate antineoplastic cisplatin-prodrug (designated as PCT@HCCT) via hydrophobic interactions and π - π stacking forces during the self-assembly process (Scheme 1A). The matrix of the HCCT micelle is the HA-ss-Ce6-TPP polymer, in which the hyaluronic acid (HA) that possesses good biocompatibility as the hydrophilic block can improve micellar internalization in tumor cells owing to HA receptor-mediated endocytosis.

Moreover, it can be degraded in the presence of hyaluronidase (HAase).²⁸ TPP modified Ce6 is grafted on cystamine-modified HA (HA-CYS) via an amide bond as the hydrophobic block, in which Ce6 can target mitochondria via the TPP function and produce ROS *in situ* under light irradiation (wavelength of 650 nm) to effectively decrease membrane potential ($\Delta\Psi_m$) and improve the mitochondrial membrane permeability. The hydrophilic and hydrophobic segments are linked with disulfide bonds (SS), which can be cleaved in the presence of high levels of glutathione (GSH).²⁹⁻³¹ In addition, cisplatin was employed as a model antitumor drug, and it was prepared as prodrug cisplatin (PCT) that consisted of three distinct components. The first was a mitochondria-targeting agent, TPP, which displayed a dramatic enhancement of accumulation of PCT around the mitochondrial membrane. The second is the photosensitizer Ce6 for producing ROS under light irradiation. The third is the anticancer drug, which could induce cellular apoptosis by depolarizing mitochondrion after its conversion to cisplatin with the endogenous reductants (e.g., glutathione, GSH).^{32,33} Scheme 1B shows that once the PCT-loaded

HCCT micelles accumulated in tumor tissue through the EPR effect, they could be internalized by tumor cells *via* CD44 receptor-mediated targeting. Subsequently, the HA layer will undergo digestion into small conjugated pieces by HAase, which has the greatest activity in acid *endo*/lysosomes.²⁸ Concurrently, light irradiation induces ROS generation, which could disrupt the *endo*/lysosomal membranes to release PCT into the cytoplasm,^{34,35} thus rapidly targeting the mitochondria *via* the TPP function and allowing conversion to free cisplatin through redox-responsiveness.^{32,33} At the same time, the membrane permeability of mitochondria would be improved by the generated ROS, thus allowing the entry of cisplatin into the mitochondria that causes mitochondrial damage, ultimately resulting in mitochondria-mediated apoptosis. Scheme 1C illustrates the corresponding changes in the chemical structure of the polymer HCCT owing to the sequential HAase and redox-responsive effects and to the chemical structure of the prodrug PCT.

Results and discussion

The prodrug PCT and the polymer HCCT were synthesized in accordance with the procedures shown in Fig. 1A. Briefly, the prodrug PCT was first synthesized *via* an acylation reaction

between the $-NH_2$ group of the *N*-Boc-ethylenediamine modified Pt-COOH (Pt-NH-NH-Boc) and the $-COOH$ group of the TPP modified Ce6 (TPP-Ce6). To improve the biocompatibility and enhance the membrane-targeting ability of prodrug PCT, the cystamine modified HA (HA-CYS) provided an $-NH_2$ group to further conjugate TPP-Ce6 *via* an acylation reaction to obtain a membrane-targeted polymer (HCCT). The latter could be used for loading PCT *via* hydrophobic interactions and π - π stacking forces developed in the process of self-assembly. Furthermore, the purified intermediates and final products were characterized using 1H nuclear magnetic resonance (1H NMR) or Fourier-transform infrared (FT-IR) spectroscopy (Fig. 1B and C, and Fig. S1 and S2 in the ESI[†]). The presence of the peaks for the characteristic groups of the aromatic ring group of TPP (7.71–7.80 ppm), the double-bond group of Ce6 (6.16–6.45 ppm), the *N*-acetyl group of HA (2.0 ppm), and the amidogen group of Pt-NH₃ (6.53 ppm) were confirmed in the 1H NMR spectra (Fig. 1B and C), thus indicating that HCCT and PCT were successfully synthesized.

The blank micelles (HCCT) and PCT-loaded HCCT micelles (PCT@HCCT) were fabricated using a dialysis method. In transmission electron microscopy (TEM) images (Fig. 2A and B), both HCCT and PCT@HCCT present a well-dispersed and

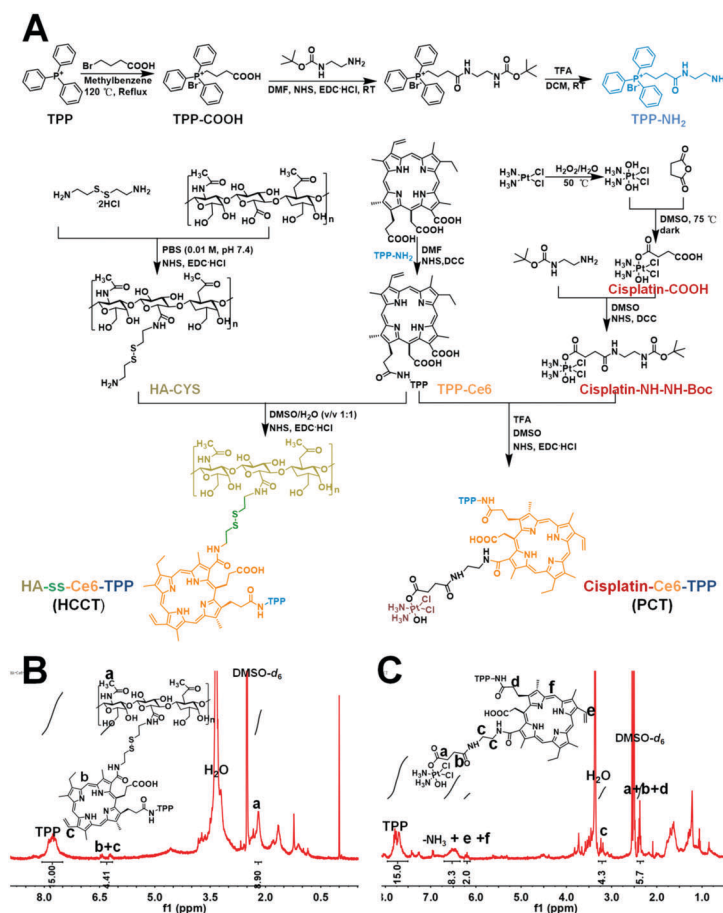


Fig. 1 (A) Synthetic route and chemical structure of HCCT conjugate and prodrug PCT. (B) 1H NMR spectrum of HCCT in DMSO-*d*₆: δ 7.80–7.71 (m, TPP), 6.18–6.45 (m, $-CH=CH_2$, $3 \times -CH=C_2NH-$), 2.0 (s, CH_3CO-) and (C) PCT in DMSO-*d*₆: δ 7.81–7.68 (m, TPP), 6.57–6.16 (m, $2 \times -NH_3$), $-CH=CH_2$, $3 \times -CH=C_2NH-$), 3.26–3.19 (m, $-NH-CH_2-$ and $-CH_2-NH-$), 2.42–2.35 (m, $-CO-CH_2-CH_2-CO-$ and $-CH_2-CH_2-CO-$).

homogeneous core-shell structure. In the ^1H NMR spectra in D_2O (Fig. 2C), the characteristic peaks of the hydrophobic TPP-Ce6 block disappeared, however, the peaks of the hydrophilic HA still remained, confirming the core-shell structure of PCT@HCCT with TPP-Ce6 in the core and HA within the shell. After the PCT was loaded, the hydrodynamic size of HCCT slightly increased from 110 to 124 nm, and the zeta potential changed from -15 to -8 mV, because HCCT with a negative charge was neutralized by the positive charge of PCT (Fig. 2D). The size and surface charge of the micelle made it suitable as a nanocarrier for delivering anticancer drugs since it has been reported that nanoparticles (<200 nm) have a better chance of accumulating in solid tumors *via* an enhanced permeability and retention (EPR) effect.^{36,37} The PCT loading content (PCT/HCCT, w/w) improved with the increasing feeding ratio of PCT/HCCT (Table S1, ESI †). Based on the optimization, PCT@HCCT achieved an increased PCT loading content that equalled 15.3 wt% (PCT/HCCT, w/w), and the feeding PCT:HCCT weight ratio of 0.25:1 was used for the following experiments.

The UV-vis-NIR spectrum revealed the characteristic peaks of Ce6 (404 and 650 nm) for PCT and HCCT, indicating the successful conjugation of Ce6-TPP to HA-CYS. After PCT was loaded into HCCT, the characteristic peaks of Ce6 were red-shifted (Fig. 2E). Based on the calculations with the use of the

spectrum, 33.17 wt% of the Ce6 molecules was conjugated to the polymer, which was validated *via* the grafting rate of Ce6 ($\lambda = 405$ nm) in DMSO (Fig. S4, ESI †). The same results could be calculated using ^1H NMR data in Fig. 1B. Interestingly, from the fluorescence spectroscopy results (Fig. 2F), HCCT and PCT@HCCT showed negligible fluorescence intensity at this excitation wavelength, thus suggesting that the increased density of Ce6 in the micelles remained in a self-quenched state from the perspective of fluorescence.³⁸

We then investigated the feasibility of HAase to stimulate fluorescence activation of PCT@HCCT. As displayed in Fig. 2G, the fluorescence of PCT@HCCT could be activated by degrading the backbone of HA when it was incubated with HAase (0.5 mg mL^{-1}). Furthermore, the HAase-induced response behavior was further investigated based on DLS analysis. As shown in Fig. 2H and Fig. S5 (ESI †), when incubated in PBS, H_2O , or RPMI 1640 cell culture medium containing 10% fetal bovine serum (FBS) without HAase for 7 d, the size of the PCT@HCCT micelle did not show any change, thus implying that the micelle was stable within the blood circulation. However, when it was incubated with 0.5 mg mL^{-1} HAase for 12 h, the micelle size distribution changed from the originally unimodal peak to multimodal peaks (Fig. 2I). The result further demonstrated that the backbone of HA could have been

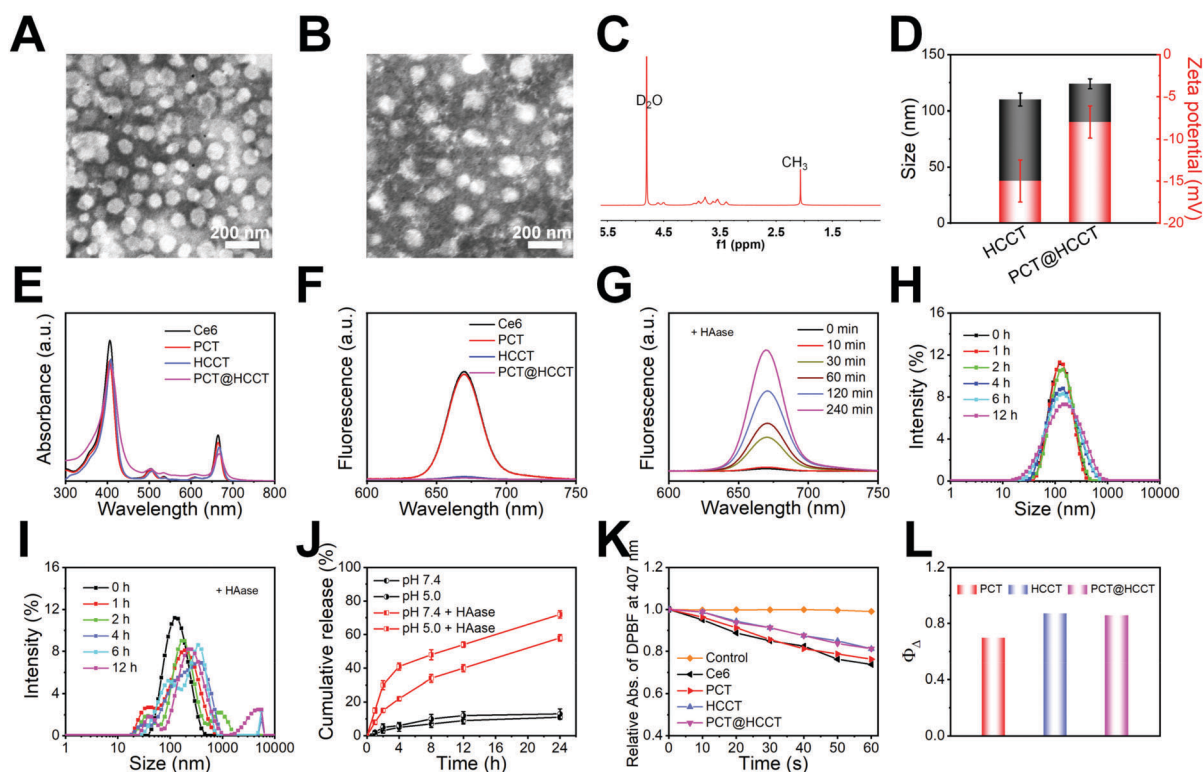


Fig. 2 Characterization of the formation and cascade-responsive behaviors of the micelle. (A) TEM image of HCCT micelles and (B) PCT@HCCT micelles. (C) ^1H NMR spectrum of PCT@HCCT in D_2O . (D) Particle size and zeta potential of the HCCT and PCT@HCCT micelles. (E) UV-vis spectrum and fluorescence spectra (F) of free Ce6, PCT, HCCT and PCT@HCCT micelles in DMSO or distilled water. (G) HAase-induced fluorescence emission changes of PCT@HCCT micelles in phosphate buffer solution (PBS) with HAase at different times. (H) The size distribution of HCCT micelles in PBS at different times. (I) HAase-induced size changes of HCCT micelles at different times. (J) *In vitro* PCT release from PCT@HCCT micelles after incubation with different simulated environments at 37°C . (K) Relative absorbance profile at 407 nm of DPBF in different samples in PBS solution after irradiation with light every 10 s. (L) Singlet oxygen quantum yield (Φ_Δ) of the different samples.

degraded by HAase. The final purposes in the development of drug delivery systems in cells include the controlled drug delivery and its release. Thus, to confirm the enhancement of the PCT release from the PCT@HCCT micelle triggered by HAase, the released amount of PCT was quantified with inductively coupled plasma mass spectrometry (ICP-MS), by detecting the content of Pt using a dialysis bag in a simulated environment of the cytoplasm. In Fig. 2J, when HAase was introduced into the buffer solutions at a pH of 7.4 or 5.0, the PCT release rate was accelerated compared with the rate at a corresponding pH value without HAase. For instance, the PCT release percentages from PCT@HCCT increased from 8% in 1 h to 58% in 24 h at pH = 7.4 with HAase, and increased from 15% in 1 h to 72% in 24 h at pH = 5.0 with HAase. The results also indicated that the outer shell of HA can be degraded into small pieces by HAase, which is highly active in acidic tumor microenvironments,²⁸ thus leading to a significant reduction in the spatial barrier of the micelles.

To study the light-triggered singlet oxygen ($^1\text{O}_2$) generation and singlet oxygen quantum yield (Φ_Δ), 1,3-diphenylisobenzofuran (DPBF) was selected as an indicator for which absorption was irreversibly quenched by $^1\text{O}_2$.³⁹ As shown in Fig. 2K, the

relative absorbance of DPBF in the PCT@HCCT PBS solution decreased by 18.8% with 650 nm light irradiation within 60 s. The rapid decrease of absorbance of DPBF suggested that $^1\text{O}_2$ was efficiently produced by PCT@HCCT, and that the $^1\text{O}_2$ quantum yield in the PBS solution was 0.86, which was 1.34-fold higher than that of free Ce6 (0.64) (Fig. 2L and Fig. S6, ESI[†]).

The intracellular uptake and light-activated ROS generation of the micelles were examined in murine B16F10 cells. Since the HA ligand shows an increased binding affinity to the CD44 receptor, strong interactions between the CD44 receptor on the membranes of B16F10 cells and HA-coordinated ligands are expected. As shown in Fig. S7B (ESI[†]), the adsorption behavior of B16F10 cells to PCT@HCCT was studied using a quartz crystal microbalance (QCM) (Q-Sense Explorer, Biolin Scientific, Sweden). Since the mass change on the electrode surface is proportional to the frequency shift of the output oscillation, the frequency shift attributed to interactions between the gold electrode and cells reached 3.7 Hz after the injection of B16F10 cells. However, when B16F10 cells were pretreated with molecular HA, the frequency shift increased to 4.7 Hz, thus indicating a significant enhancement in the cell affinity of PCT@HCCT by HA coordination. Additionally, B16F10 cell internalization of

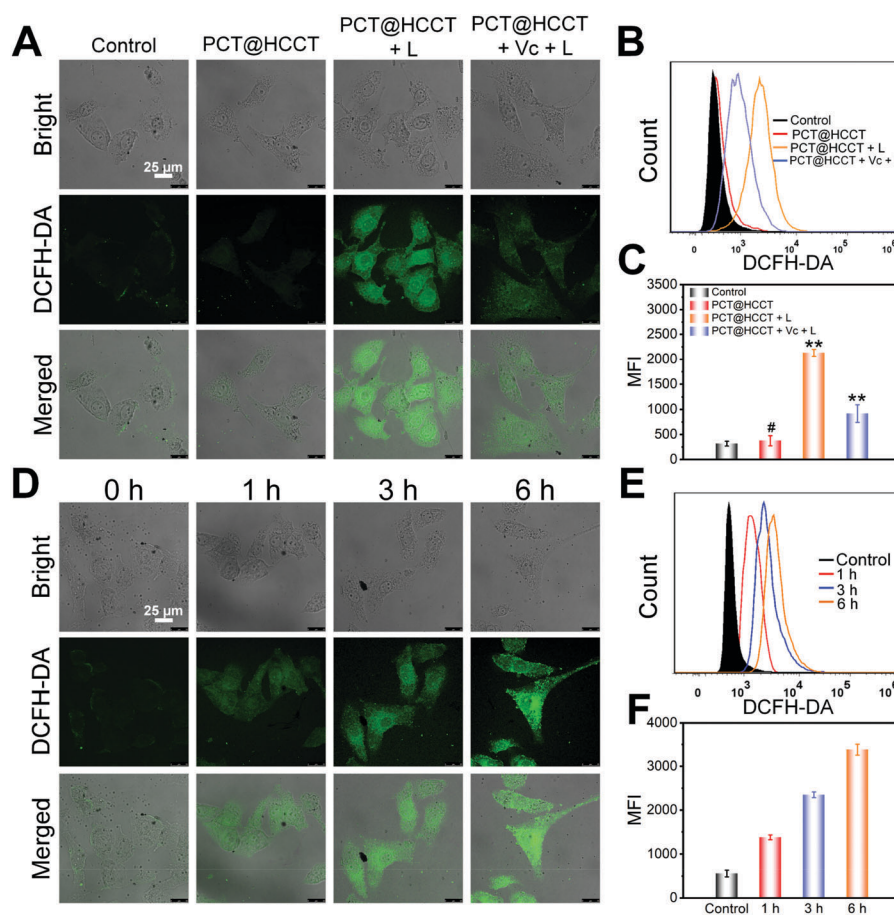


Fig. 3 ROS production by PCT@HCCT micelles. (A) CLSM images of PCT@HCCT micelle-induced ROS generation in B16F10 cells under various conditions. (B) and (C) Flow cytometric examination of intracellular ROS generation of PCT@HCCT induced in B16F10 cells under various conditions. (D) CLSM images of PCT@HCCT micelle-induced ROS generation in B16F10 cells for different times. (E) and (F) Flow cytometric examination of intracellular ROS generation of PCT@HCCT induced in B16F10 cells for different times. ** $p < 0.01$ and # $p > 0.05$ vs. control ($n = 3$).

PCT@HCCT was analyzed *via* confocal laser scanning microscopy (CLSM) and flow cytometric examinations. As shown in Fig. S7A, B, and D (ESI[†]), B16F10 cells incubated with PCT@HCCT with light irradiation displayed remarkably increased fluorescence, which was approximately 2.2-fold higher than the mean fluorescence intensity (MFI) in comparison to that without light irradiation. Additionally, when the cells were pretreated with molecular HA, the internalization of PCT@HCCT was decreased. The same result can also be found in Fig. S7E (ESI[†]), which shows the Pt concentration in cells *via* ICP-MS detection. These results confirmed that the internalization of PCT@HCCT can be effectively improved *via* CD44 receptor-mediated endocytosis⁴⁰ and photochemical internalization (PCI).⁴¹

We also investigated the intracellular light-triggered ROS generation of PCT@HCCT using CLSM and flow cytometry. The B16F10 cells were treated with PCT@HCCT with or without light irradiation, and the levels of ROS were subsequently measured using ROS detection probes (DCFH-DA). After light irradiation, the bright fluorescence of ROS production (green color) in the PCT@HCCT-treated cells was observed by CLSM (Fig. 3A), thus indicating that light induced significant ROS generation inside the cells that led to a 5.7-fold increase of MFI compared to that without light irradiation (Fig. 3B and C). However, ROS generation was suppressed when the cells were pre-incubated with ROS scavenger vitamin C (Vc). Additionally, the fluorescence intensity increased in a time-dependent manner (Fig. 3D), which is approximately equivalent to a 2.5-fold increase of MFI after the B16F10 cells were treated with PCT@HCCT for 6 h compared to 1 h treatment (Fig. 3E and F). These results demonstrated that the ROS can be generated only under light irradiation.

We then examined the cytotoxicity of PCT@HCCT on B16F10 cells using live/dead staining with the Alamar blue assay. PBS with light irradiation was used as the control. Fig. S9 (ESI[†]) shows that the cell viability was >90% for both HUVEC cells (normal cells) and B16F10 (tumor cells) after incubation with the nanocarriers (HCCT) with concentrations in the range 10–250 $\mu\text{g mL}^{-1}$ for 24 h, thus indicating that the blank micelles had excellent cytocompatibility. Fig. S10A (ESI[†]) shows that PCT@HCCT with light irradiation was more toxic (IC_{50} of PCT is 0.421 μM) compared to that without light irradiation (IC_{50} of PCT is 1.63 μM), but the toxicity effect was weakened when the cells were pre-incubated with the ROS scavenger Vc. This difference is attributed to the ROS generation by Ce6 in PCT@HCCT under light irradiation. Live/dead staining was performed to further evaluate the light-dependent cytotoxicity, and the result was consistent with the Alamar blue assay since more cells died when they were treated with PCT@HCCT under light irradiation (Fig. S10B, ESI[†]).

An annexin V-FITC/propidium iodide (PI) double-staining assay was used to evaluate the apoptosis in B16F10 cells induced by PCT@HCCT under different processing conditions. Compared to the treatment without light irradiation (a total apoptotic ratio of 53.03%), the percentage of B16F10 cells undergoing apoptosis after incubation with PCT@HCCT with light irradiation (a total apoptotic ratio of 83.24%) was significantly increased (Fig. S10C and D, ESI[†]). Similar to the

cytotoxicity study, cells exposed to PCT@HCCT showed light-independent apoptotic characteristics. Therefore, it can be concluded that PCT@HCCT was able to induce more cell apoptosis and death upon light stimulus.

To verify whether the prodrug can effectively escape lysosomes, lysosomal escape of prodrug in B16F10 cells was visualized using CLSM. As shown in Fig. S11 (ESI[†]), after PCT@HCCT is internalized by the cells, hyaluronic acid is degraded by hyaluronidase in lysosomes, which could lead to part of PCT being released from PCT@HCCT and diffusing freely into the cytoplasm. In addition, because internalization of PCT@HCCT can be effectively improved by photochemical internalization (PCI), the red fluorescence of Ce6 is stronger with light than without light at the same time. Moreover, the reactive oxygen, which was produced by Ce6 under light, can destroy the lysosome structure, so green fluorescence (lysosomes) was weaker with light than without light, thus suggesting that light irradiation cannot only improve the amount of internalization of PCT@HCCT, but it can also accelerate prodrug escape from lysosomes and distribution in the cytoplasm.⁴² Furthermore, the co-localization analysis of mitochondria was utilized to observe the targeting of the prodrug to the mitochondria. Fig. 4A1 and A2 show the CLSM images of the B16F10 cells treated with PCT@HCCT with light irradiation (10 min) after incubation for 1 and 6 h, respectively. The corresponding fluorescence intensity profiles across the white line (marked in the CLSM images) are shown in Fig. 4B1 and B2. Quantitative analysis of the fluorescence intensity and subcellular co-localization analysis were derived from these fluorescence images. Pearson's correlation coefficient (R_r) was utilized to quantitatively evaluate the correlation between the two types of fluorescence co-localization analysis.⁴³ According to this, we can quantitatively determine whether the prodrug is able to target the mitochondria effectively after the cells were incubated with PCT@HCCT for 1 or 6 h. As shown in Fig. 4C, the mean R_r values of the red (Ce6) and the green fluorescence (MitoTracker green) at 1 and 6 h were 0.87 and 0.92, respectively, thus indicating that there were no obvious differences of co-localization after incubation for 1 and 6 h. The results also illustrated that the prodrug that escaped from lysosomes could rapidly accumulate around the mitochondria.

The TEM images in Fig. 4D1–D3 and D5–D7 show the intracellular transport process of cisplatin in PCT@HCCT in B16F10 cells at 6 h. As shown in the magnified images, cisplatin could enter the mitochondria in the B16F10 cells after incubation with PCT@HCCT and following light irradiation. However, no cisplatin could be found in the mitochondria of the B16F10 cells after incubation with PCT@HCCT but without the use of light irradiation. This result further confirms that chemotherapeutic drugs struggle to pass through the complete mitochondrial double membrane structure.¹⁷ In addition, the presence of platinum was confirmed based on energy dispersive spectrometry (EDS) analysis of the two groups (Fig. 4D4 and D8). Additionally, only platinum was detected in the mitochondria of B16F10 cells in the case of PCT@HCCT in the light irradiation group, thus illustrating that cisplatin entered mitochondria after the membrane permeability was improved using *in situ* ROS generation following light irradiation.

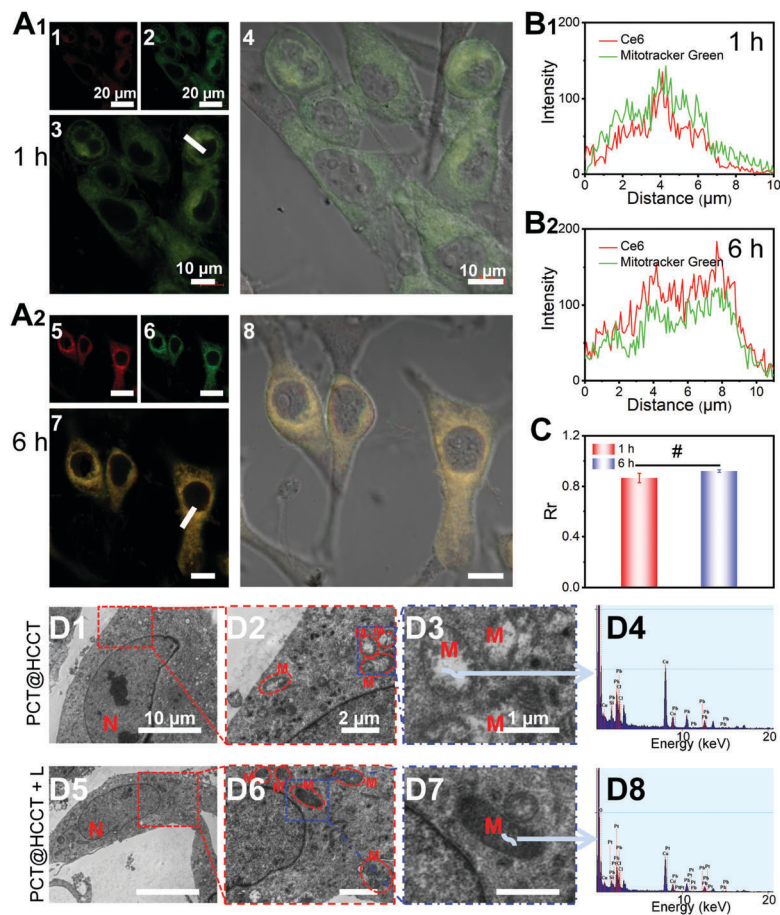


Fig. 4 Mitochondrial co-localization analysis. (A1) Confocal images of B16F10 cells after incubation with PCT@HCCT micelles with irradiation (10 min) for (A1 or A2) 6 h. (B1 and B2) Profiles of the distribution of the fluorescence signals of Ce6 (Red) and MitoTracker Green along the signified white line in the confocal microscopic images. (C) Co-localization ratio between Ce6 and MitoTracker Green signified by the R_r value after the B16F10 cells were incubated with PCT@HCCT micelles with irradiation (10 min) for 1 and 6 h. (D1–D3) and (D5–D7) Mitochondria ultrastructure observed by using TEM. (D1–D3) B16F10 cells were incubated with PCT@HCCT micelles without irradiation and (D5–D7) with irradiation (10 min). (D4 and D8) Elemental analysis of mitochondria. N: nucleus; M: mitochondria. In (A1 and A2), 1 and 5: red fluorescence of Ce6, 2 and 6: green fluorescence of $\#p > 0.05$ ($n = 5$).

To further investigate the mechanism of how PCT@HCCT in the presence of light irradiation induced cell apoptosis, we systematically studied the changes in mitochondrial membrane potential and the expression of related proteins in B16F10 following light irradiation. Fluorescent probe JC-1 staining was used to monitor the change in mitochondrial membrane potential ($\Delta\Psi_m$).⁴⁴ When the permeability of the mitochondrial membrane increases, $\Delta\Psi_m$ will decrease.⁴⁵ When the mitochondria are normal with an intact mitochondrial membrane system, JC-1 will display potential-dependent accumulation in the mitochondrial matrix, which is accompanied by red fluorescence emission owing to the formation of J-aggregates, thus indicating an increased $\Delta\Psi_m$. In contrast, depolarized mitochondria display green fluorescence owing to the formation of J-monomers in the cytoplasm, thereby indicating a lower $\Delta\Psi_m$.⁴⁶ Therefore, the change in membrane potential can be evaluated by measuring the green/red fluorescence intensity ratio. Fig. 5A demonstrates that PCT@HCCT without light irradiation has a negligible influence on the mitochondrial membrane potential. The mitochondria were depolarized with light irradiation as indicated by

a noticeable increase of the green fluorescence intensity due to the collapse of the mitochondrial $\Delta\Psi_m$. The intensity of the green fluorescence further decreased when the cells were pre-incubated with a ROS scavenger Vc. Quantitative analysis of the ratio between the green-to-red fluorescence using flow cytometric measurements confirmed that PCT@HCCT significantly caused mitochondrial depolarization (Fig. 5B and C). This result indicates that the prodrug can localize in the mitochondria, and the local ROS of the organelles subsequently increase rapidly with light irradiation, further leading to a rapid decrease in $\Delta\Psi_m$ owing to the fact that the mitochondria are sensitive to ROS.⁴⁷

In comparison, the expression level of proteins was further investigated by Western blot assays (Fig. 5D) in order to evaluate whether the mitochondrial damage and the activation of the mitochondrial apoptotic pathway can be caused by the entry of cisplatin in the mitochondria and its subsequent action on mitochondrial DNA. It is known that the damage of mitochondria could cause a remarkable release of cytochrome C into the cytosol that would prompt cell apoptosis.^{48,49} Additionally, the improvement of the membrane permeability of mitochondria

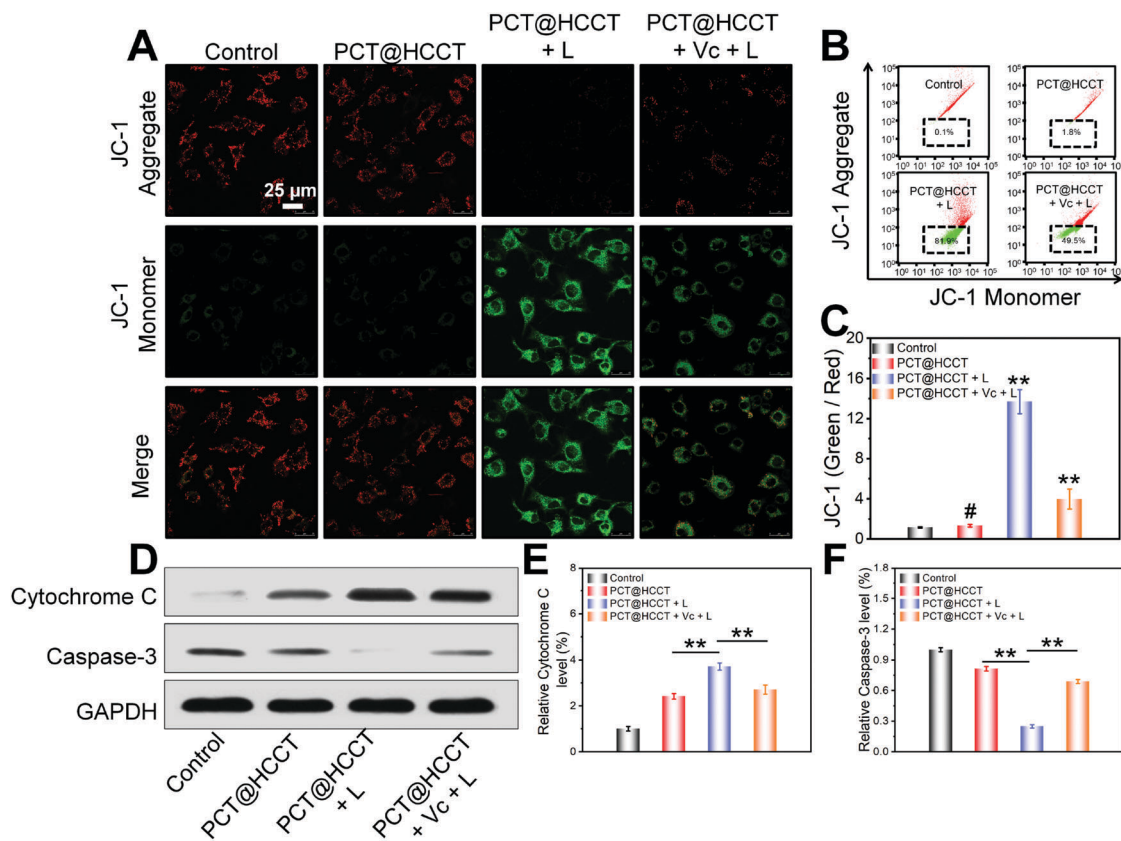


Fig. 5 Mitochondrial membrane potential ($\Delta\Psi_m$) analysis. (A) CLSM images of $\Delta\Psi_m$ shift as determined by JC-1 assay of B16F10 cells. (B) Flow cytometric curves of JC-1 distribution in B16F10 cells. (C) The JC-1 monomer to aggregate (green/red) ratio in the cells as determined by flow cytometry. $**p < 0.01$ and $\#p > 0.05$ vs. control ($n = 3$). (D) Representative cytochrome C and caspase-3 protein were analyzed by western blot. Glyceraldehyde 3-phosphate dehydrogenase (GAPDH) was used as a loading control. (E and F) Cytochrome C and caspase-3 protein relative to GAPDH were determined by Image J, respectively. $**p < 0.01$ denote statistically significant differences.

further promoted the release of cytochrome C into the cytoplasm. As shown in Fig. 5E, the cytochrome C level of PCT@HCCT was increased with light irradiation, but it decreased when the cells were pre-incubated with the ROS scavenger Vc. Meanwhile, the expression of caspase-3 and cleaved caspase-3, which is a major cell death effector protease, was also determined. The caspase-3 expression and cleaved caspase-3 level of PCT@HCCT with light irradiation were significantly downregulated and upregulated in contrast to that without light irradiation, respectively (Fig. 5F and Fig. S14B, ESI[†]), thus suggesting the occurrence of mitochondrial damage and the initiation of the mitochondria-mediated apoptotic pathway.

To explore the *in vivo* tumor-targeted capability of PCT@HCCT, B16F10 tumor bearing mice were used as a tumor xenograft model. Compared to the noncellular membrane-targeted group (PCT@mPEG-PCL), a remarkably increased fluorescence Ce6 signal was observed in the tumor region at 1, 6, and 12 h post-injection of PCT@HCCT (Fig. 6A). The tumor and normal tissues were collected for *ex vivo* imaging at 12 h, and the relative fluorescence signal of Ce6 was mainly distributed in the tumor and liver tissues (Fig. 6A). These results indicated that PCT@HCCT could accumulate at the tumor site *via* both the EPR effect and HA receptor-mediated endocytosis.

To further assess the *in vivo* anticancer efficacy of PCT@HCCT, various formulations were intravenously injected into B16F10 tumor-bearing mice every 2 days three times, including days 0, 3, and 6. The light source for therapy was a 650 nm laser producing a photodensity of 250 mW cm⁻². As shown in Fig. 6B and C, there is an effective inhibition of tumor growth in mice treated with PCT@HCCT using light irradiation. At day 15, PCT@HCCT without light irradiation and PCT@mPEG-PCL with light irradiation displayed moderate anticancer capability with the tumor volumes of 1.68 and 1.24 cm³, respectively. However, PCT@HCCT with light irradiation displayed significantly higher inhibitory effects on tumor growth, and the tumor volume was only 0.51 cm³. The inhibition rate of the tumor growth in the PCT@HCCT and light irradiation group is 84.4%, which is 1.7-fold higher than that in the PCT@HCCT group without the use of light irradiation (49.6%), and 1.3-fold higher than that in the PCT@mPEG-PCL and light irradiation group (62.8%). The therapeutic efficacy of PCT@HCCT was further evaluated by histological examination. The images of hematoxylin and eosin (HE) stained tumor tissue treated by PCT@HCCT with light irradiation indicated the presence of a large range of dead cells without nuclei (Fig. 6F). Additionally, deoxynucleotidyl transferase dUTP nick-end labeling (TUNEL)

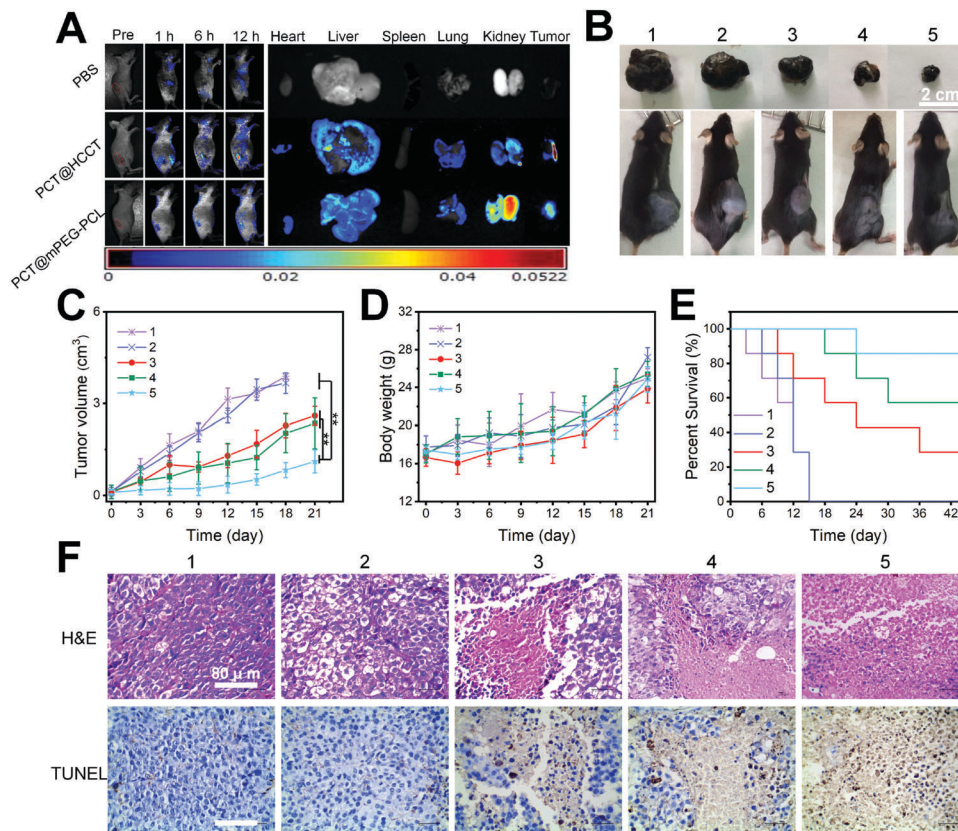


Fig. 6 *In vivo* antitumor therapy. (A) *In vivo* fluorescence images of B16F10 tumor bearing nude mice after intravenous injection of PCT@HCCT and PCT@mPEG-PCL, and *ex vivo* fluorescence images of isolated tissues at 12 h post-injection. (B) Excised B16F10 tumors (15th d after the first treatment) from tumor-bearing C57BL/6 mice subjected to different treatments. (C) Tumor size, (D) body weight changes, and (E) survival curves. (F) *Ex vivo* histological analyses of tumor sections. In hematoxylin and eosin-stained sections, nuclei are stained blue and the extracellular matrix and cytoplasm are stained red. In terminal deoxynucleotidyl transferase dUTP nick end labeling analysis, blue and brown stains indicate normal and apoptotic cells, respectively. In (B–F), (1): PBS + L; (2): HCCT; (3): PCT@HCCT; (4): PCT@mPEG-PCL + L; (5): PCT@HCCT + L. ** $p < 0.01$ denote statistically significant differences.

staining (Fig. 6F) was also employed to evaluate the tumor cell apoptosis caused by various formulations, where the group treated with PCT@HCCT and light appeared to have the highest level of cell apoptosis in tumor tissues. Collectively, these results verified that the effect of antitumor therapy of PCT@HCCT can be significantly improved under light irradiation, owing to the capabilities of targeted mitochondria therapy with nanocarriers.

To evaluate the *in vivo* safety of the nanocarrier, the mice body weight, survival rate, and histological analyses of organs were assessed. All groups showed no significant change in mice body weight during the treatment (Fig. 6D). Furthermore, the survival rate of mice in the PCT@HCCT and light group was the highest (85.7%) among all groups during a period of 45 d (Fig. 6E), thus implying that this was the safest treatment. General body toxicity was further evaluated by HE staining of the major organs (*e.g.*, heart, liver, spleen, lung, and kidney). The HE-stained images in Fig. S15 (ESI[†]) show that there were no appreciable histological changes and undetectable adverse effects (*e.g.*, inflammatory response or necrosis) in the main organs, thus indicating excellent biocompatibility *in vivo*. Therefore, the micelle is an excellent nanoformulation for

cancer therapy because it possesses both high antitumor efficacy and low-systemic toxicity.

Conclusions

In summary, we successfully developed a new, dual-targeted, cascade-responsive multifunctional micelle to specifically induce mitochondrial apoptosis in cancer therapy. The drug loading content of this micelle was significantly enhanced *via* hydrophobic interactions and π - π stacking forces developed between the micellar matrix and the drug molecules. The micelle could be selectively internalized by tumor cells through membrane-targeting, and the HA layer could be subsequently degraded into small conjugated pieces by hyaluronidase. Concurrently, the ROS generated from light irradiation disrupted the *endo*/lysosomal membranes to prompt the release of PCT, which possessed a considerable capacity in targeting the mitochondria owing to the TPP function and conversion into free cisplatin through the redox-responsive effect in the cytoplasm. Simultaneously, the membrane permeability of the mitochondria could be effectively improved by the generated ROS, thus

allowing cisplatin to enter the mitochondria and cause mitochondrial damage, ultimately resulting in mitochondrial apoptosis. As a result, the micelle represented a highly effective anticancer efficacy with a tumor growth inhibition rate of 84.4% and a survival rate of 85.7% in mice. Therefore, the dual-targeted and cascade-responsive multifunctional micelles are envisaged to be a promising nanocarrier for mitochondrial therapy of malignant tumors.

Conflicts of interest

The authors declare no competing financial interest.

Acknowledgements

This work was partially supported by the China National Funds for Distinguished Young Scientists (51725303), the National Natural Science Foundation of China (21574105, 81701831, and 51703189), the Sichuan Province Youth Science and Technology Innovation Team (2016TD0026) and Doctoral Innovation Fund Program of Southwest Jiaotong University (D-CX201730).

References

- 1 S. Fulda, L. Galluzzi and G. Kroeme, *Nat. Rev. Drug Discovery*, 2010, **9**, 447.
- 2 B. P. Shah, N. Pasquale, G. De, T. Tan, J. Ma and K.-B. Lee, *ACS Nano*, 2014, **8**, 9379.
- 3 Y. Zhang, Y. Shen, X. Teng, M. Yan, H. Bi and P. C. Morais, *ACS Appl. Mater. Interfaces*, 2015, **7**, 10201.
- 4 X. Guo, X. Wei, Y. Jing and S. Zhou, *Adv. Mater.*, 2015, **27**, 6450.
- 5 K. Han, W. Y. Zhang, J. Zhang, Q. Lei, S. B. Wang, J. W. Liu, X. Z. Zhang and H. Y. Han, *Adv. Funct. Mater.*, 2016, **26**, 4351.
- 6 J. Wang, S. Shen, D. Li, C. Zhan, Y. Yuan and X. Yang, *Adv. Funct. Mater.*, 2018, **28**, 1704806.
- 7 K. Han, J. Y. Zhu, H. Z. Jia, S. B. Wang, S. Y. Li, X. Z. Zhang and H. Y. Han, *ACS Appl. Mater. Interfaces*, 2016, **8**, 25060.
- 8 K. Han, Q. Lei, S. B. Wang, J. J. Hu, W. X. Qiu, J. Y. Zhu, W. N. Yin, X. Luo and X. Z. Zhang, *Adv. Funct. Mater.*, 2015, **25**, 2961.
- 9 H. C. Wang, S. C. Hsieh, J. H. Yang, S. Y. Lin and L. Y. Sheen, *Nutr. Cancer*, 2012, **64**, 770.
- 10 K. S. Eom, H. J. Kim, H. S. So, R. Park and T. Y. Kim, *Biol. Pharm. Bull.*, 2010, **33**, 1644.
- 11 S. Zhu, J. Jin, Y. Wang, Z. Ouyang, C. Xi, J. Li, Y. Qiu, J. Wan, M. Huang and Z. Huang, *Food Chem. Toxicol.*, 2012, **50**, 1149.
- 12 X. Hu, S. Zhai, G. Liu, D. Xing, H. Liang and S. Liu, *Adv. Mater.*, 2018, **30**, 1706307.
- 13 X. Guo, L. Wang, K. Duval, J. Fan, S. Zhou and Z. Chen, *Adv. Mater.*, 2018, **30**, 1705436.
- 14 Y. Wang, L. Zhang, X. Zhang, X. Wei, Z. Tang and S. Zhou, *ACS Appl. Mater. Interfaces*, 2016, **8**, 5833.
- 15 Z. T. Cao, Z. Y. Chen, C. Y. Sun, H. J. Li, H. X. Wang, Q. Q. Cheng, Z. Q. Zuo, J. L. Wang, Y. Z. Liu, Y. C. Wang and J. Wang, *Biomaterials*, 2016, **94**, 9.
- 16 S. Marrachea, R. K. Pathaka and S. Dhar, *Proc. Natl. Acad. Sci. U. S. A.*, 2014, **111**, 10444.
- 17 S. R. Jean, M. Ahmed, E. K. Lei, S. P. Wisnovsky and S. O. Kelley, *Acc. Chem. Res.*, 2016, **49**, 1893.
- 18 Y. Wang, G. Wei, X. Zhang, X. Huang, J. Zhao, X. Guo and S. Zhou, *Small*, 2018, **14**, 1702994.
- 19 J. Xu, F. Zeng, H. Wu, C. Hu and S. Wu, *Biomacromolecules*, 2014, **15**, 4249.
- 20 S. Biswas and V. P. Torchilin, *Adv. Drug Delivery Rev.*, 2014, **66**, 26.
- 21 B. F. Zhang, L. Xing, P. F. Cui, F. Z. Wang, R. L. Xie, J. L. Zhang, M. Zhang, Y. J. He, J. Y. Lyu, J. B. Qiao, B. A. Chen and H. L. Jiang, *Biomaterials*, 2015, **61**, 178.
- 22 Y. Tan, Y. Zhu, Y. Zhao, L. Wen, T. Meng, X. Liu, X. Yang, S. Dai, H. Yuan and F. Hu, *Biomaterials*, 2018, **154**, 169.
- 23 G. Yu, D. Wu, Y. Li, Z. Zhang, L. Shao, J. Zhou, Q. Hu, G. Tang and F. Huang, *Chem. Sci.*, 2016, **7**, 3017.
- 24 B. Feng, F. Zhou, Z. Xu, T. Wang, D. Wang, J. Liu, Y. Fu, Q. Yin, Z. Zhang, H. Yu and Y. Li, *Adv. Funct. Mater.*, 2016, **26**, 7431.
- 25 R. A. J. Smith, C. M. Porteous, A. M. Gane and M. P. Murphy, *Proc. Natl. Acad. Sci. U. S. A.*, 2003, **100**, 5407.
- 26 M. Ethirajan, Y. Chen, P. Joshi and R. K. Pandey, *Chem. Soc. Rev.*, 2011, **40**, 340.
- 27 Z. Yu, Q. Sun, W. Pan and Na. Li and B. Tang, *ACS Nano*, 2015, **9**, 11064.
- 28 R. Stern and M. J. Jędrzejak, *Chem. Rev.*, 2006, **106**, 818.
- 29 X. Guo, C. Shi, G. Yang, J. Wang, Z. Cai and S. Zhou, *Chem. Mater.*, 2014, **26**, 4405.
- 30 C. Shi, X. Guo, Q. Qu, Z. Tang, Y. Wang and S. Zhou, *Biomaterials*, 2014, **35**, 8711.
- 31 J. Wang, G. Yang, X. Guo, Z. Tang, Z. Zhong and S. Zhou, *Biomaterials*, 2014, **35**, 3080.
- 32 Y. R. Zheng, K. Suntharalingam, T. C. Johnstone, H. Yoo, W. Lin, J. G. Brooks and S. J. Lippard, *J. Am. Chem. Soc.*, 2014, **136**, 8790.
- 33 P. Ma, H. Xiao, C. Yu, J. Liu, Z. Cheng, H. Song, X. Zhang, C. Li, J. Wang, Z. Gu and J. Lin, *Nano Lett.*, 2017, **17**, 928.
- 34 C. Qian, P. Feng, J. Yu, Y. Chen, Q. Hu, W. Sun, X. Xiao, X. Hu, A. Bellotti, Q. D. Shen and Z. Gu, *Angew. Chem., Int. Ed.*, 2017, **56**, 2588.
- 35 H. He, S. Ji, Y. He, A. Zhu, Y. Zou, Y. Deng, H. Ke, H. Yang, Y. Zhao, Z. Guo and H. Chen, *Adv. Mater.*, 2017, **29**, 1606690.
- 36 H. Maeda, J. Wu, T. Sawa, Y. Matsumura and K. Hori, *J. Controlled Release*, 2000, **65**, 271.
- 37 G. Wei, Y. Wang, X. Huang, H. Hou and S. Zhou, *Small Methods*, 2018, 1700358.
- 38 L. Feng, D. Tao, Z. Dong, Q. Chen, Y. Chao, Z. Liu and M. Chen, *Biomaterials*, 2017, **127**, 13.
- 39 X. Zhen, C. Zhang, C. Xie, Q. Miao, K. L. Lim and K. Pu, *ACS Nano*, 2016, **10**, 6400.

- 40 Y. Zhong, J. Zhang, R. Cheng, C. Deng, F. Meng, F. Xie and Z. Zhong, *J. Controlled Release*, 2015, **205**, 144.
- 41 B. S. J. M. I. Touhid, *J. Cancer Res. Exp. Oncol.*, 2011, **3**, 26.
- 42 Y. Wang, T. Yang, H. Ke, A. Zhu, Y. Wang, J. Wang, J. Shen, G. Liu, C. Chen, Y. Zhao and H. Chen, *Adv. Mater.*, 2015, **27**, 3874.
- 43 Y. Wang, G. Wei, X. Zhang, F. Xu, X. Xiong and S. Zhou, *Adv. Mater.*, 2017, **29**, 1605357.
- 44 B. N. Desai, B. R. Myers and S. L. Schreiber, *Proc. Natl. Acad. Sci. U. S. A.*, 2002, **99**, 4319.
- 45 G. Kroemer and J. C. Reed, *Nat. Med.*, 2000, **6**, 513.
- 46 M. Okadaa, N. I. Smithb, A. F. Palonponc, H. Endoa, S. Kawataa, M. Sodeokac and K. Fujita, *Proc. Natl. Acad. Sci. U. S. A.*, 2012, **109**, 28.
- 47 H. S. Jung, J. Han, J. H. Lee, J. H. Lee, J. M. Choi, H. S. Kweon, J. H. Han, J. H. Kim, K. M. Byun, J. H. Jung, C. Kang and J. S. Kim, *J. Am. Chem. Soc.*, 2015, **137**, 3017.
- 48 M. E. Guicciardi, J. Deussing, H. Miyoshi, S. F. Bronk, P. A. Svingen, C. Peters, S. H. Kaufmann and G. J. Gores, *J. Clin. Invest.*, 2000, **106**, 1127.
- 49 J. R. J. Caruso, Jr, P. Mathieu, B. Chelladurai, X. M. Yin and D. Kessel, *Cell Death Differ.*, 2002, **9**, 934.